Long-term analysis of the urban heat island effect using multisource Landsat images considering inter-class differences in land surface temperature products

Xiong Xu [a,b,c], Haoyang Pei [a], Chao Wang [a,b,*], Qingyu Xu [a], Huan Xie [a,b], Yanmin Jin [a,b], Yongjiu Feng [a,b,c], Xiaohua Tong [a,b,c], Changjiang Xiao [a,b,c]

[a] College of Surveying and Geo-informatics, Tongji University, Shanghai 200092, China
[b] Shanghai Key Laboratory for Planetary Mapping and Remote Sensing for Deep Space Exploration, Tongji University, Shanghai 200092, China
[c] Frontiers Science Center for Intelligent Autonomous Systems, Tongji University, Shanghai 201210, China

HIGHLIGHTS

- How to build a relationship between the LST products from Landsat-7 and Landsat-8 images.
- To what extent can the fitted model at time T2 be used to replace that at time T1 for long time analysis of UHI effect?
- The spatiotemporal distribution of the UHI intensity in Shenzhen city during the period of 2014–2019.

GRAPHICAL ABSTRACT
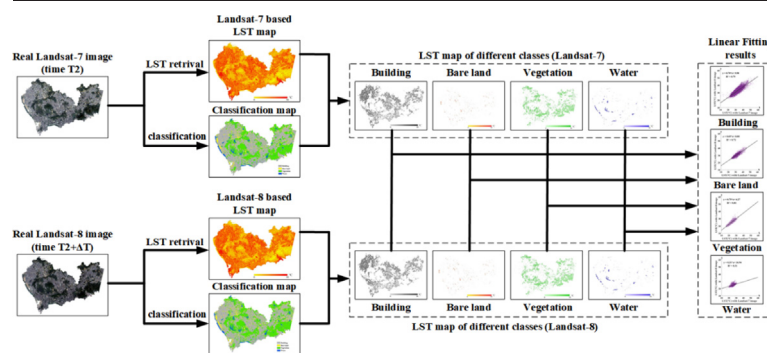
ARTICLE INFO

ABSTRACT

It is imperative to quantitatively analyze the long-term temporal and spatial characteristics of the urban heat island (UHI) effect on cities for applications, such as urban expansion and environmental protection. Owing to the high spatial resolution and availability of long time-series data, remote sensing images from Landsat satellites are widely used for land surface temperature (LST) retrieval. However, limited by the satellite revisit cycle and image quality, the use of multisource Landsat images in a long-term study of the UHI effect is inevitable. Nonetheless, owing to the differences among multisource sensors, such as Landsat-7 and Landsat-8, there may be apparent deviations in the LST results retrieved from different sensor data, which are obtained from the same area and under similar circumstances. Consequently, it is necessary to build a relationship between the LST results generated from multisource Landsat sensors for future research on the UHI effect.

In this study, Shenzhen city was studied to explore the fitting relationship between the corresponding LST products from Landsat-7 and Landsat-8 images obtained from adjacent dates with similar climatic conditions. Furthermore, factors affecting the fitting models, such as land cover types, seasonal and inter-annual differences, were analyzed. The constructed fitting model had a strong relationship with land cover types but a relatively weak relationship with seasonal and inter-annual differences; this indicates that a pseudo Landsat-8-based LST product can be generated from a Landsat-7-based LST product using a model fitted by a Landsat-7/8 pair obtained from adjacent years (or different seasons). Finally, by considering the consistency between LST products from multisource Landsat images, the spatiotemporal variations in the UHI effect in Shenzhen can be accurately explored using long time-series data.

1. Introduction

The urban heat island (UHI) effect is a phenomenon characteristic of considerably higher temperatures in urban areas than in suburban areas due to the interference with the natural ecosystem (Howard, 1833; Mohajerani et al., 2017). The UHI effect is an important environmental factor that intensifies urban high-temperature calamity and results in the deterioration of the urban environment (Hu et al., 2005). For decades, the UHI effect has gradually become a key issue, and numerous researchers have studied this effect in different regions using ground-based observations (Cheng et al., 2010). Recently, with the rapid development of thermal infrared remote sensing techniques, land surface temperature (LST) products retrieved from satellite data have become an efficient way to study the UHI effect, with the advantages of large-area coverage, spatial continuity, high efficiency, and low cost (Owen et al., 1998; Mohan et al., 2013; Xu & Chen, 2004).

Landsat data is one of the most widely used satellite data sources for UHI effect studies because of its accessibility and long-term in-orbit observations (Li et al., 2014; Zoran, 2012; Clinton & Gong, 2013; Ding & Shi, 2013; Tan & Li, 2013; Kumar et al., 2012; Estoque & Murayama, 2017; Kaplan et al., 2018; Sultana & Satyanarayana, 2020; Ren et al., 2022). Yusuf et al. (Yusuf et al., 2014) used Landsat images to retrieve the LST and land cover change products in the Kuala Lumpur Metropolis, which revealed that the urban area experienced a total increase of 8.4717 K in temperature between 1997 and 2013. Cui and Qian (Cui & Qian, 2010) studied the relationship between the UHI effect and land cover types in the city of Guangzhou using Landsat TM data from 1990, 1998, and 2005 and found that water, forest, and cultivated land play a key role in the mitigation of the UHI effect, while built-up and bare land primarily contribute to the UHI effect. Ranagalage et al. (Ranagalage et al., 2017) examined the spatiotemporal patterns of LST in the Colombo Metropolitan Area using Landsat data from 1997 to 2017 and found indications of intensifying UHI effect.

Limited by satellite revisit cycles and image quality, the use of images from different satellite sensors for the long-term study of the UHI effect is inevitable (Nichol, 2005; Yang et al., 2013; Liu, 2017; Xu et al., 2021; Sun et al., 2021). Nichol (Nichol, 2005) studied the differences in the UHI effect in Hong Kong during the day and at night using ASTER and Landsat-7 images. Yang et al. (Yang et al., 2013) used data from meteorological observation stations, MODIS, and Landsat-7 images to analyze the influence of urbanization on the UHI effect in Shijiazhuang in terms of both LST and air temperature. Liu (Liu, 2017) also analyzed the main influencing factors of spatiotemporal evolution characteristics of the UHI effect in Hefei city using Landsat and MODIS LST products. However, the possible impacts of the differences among multisource sensors on the analysis of the UHI effect have rarely been considered in previous studies. For example, there may be an apparent deviation between the generated LST products from Landsat-7 and Landsat-8 satellites for the same area under similar imaging conditions, thus negatively affecting the long-term analysis of the UHI effect. Therefore, it is essential to alleviate the inconsistencies inherent in multisource LST products for long-term applications.

In this study, Shenzhen was selected as the study area for which Landsat-7 and Landsat-8 images between 2014 and 2019 were collected. A linear model was built to represent the relationship between multisource LST products from different Landsat sensors for use in long-term studies. Furthermore, a sensitivity analysis was conducted to determine the factors affecting the fitted linear model, such as land cover types, seasonal and inter-annual differences. Finally, the rules to construct the linear model were concluded and used for the long-term analysis of the UHI effect in Shenzhen city.

The remainder of this paper is organized as follows. In Section 2, the study area is introduced and the proposed framework is presented in Section 3. The sensitivity and long-term analysis of the UHI effect for Shenzhen is detailed in Section 4. Finally, the conclusions are presented in Section 5.

2. Study area and datasets

2.1. Motivation

The inconsistencies between different Landsat sensors should be discussed first before their use in long-term applications of LST products. The mechanism of LST is complex; however, it is commonly assumed that there is a significant relationship between LST and meteorological temperature (Vancutsem et al., 2010; Mostovoy et al., 2006; Liu et al., 2013). It is further assumed that the LST for the same area under similar climatic conditions for adjacent dates should be similar. In other words, the retrieved LST products from different Landsat images, such as Landsat-7 and Landsat-8, should have high consistencies if sensor differences are not considered.

Therefore, two separate Landsat images from the Landsat-7 and Landsat-8 sensors were selected to explore the differences in the corresponding LST products. Table 1 summarizes the imaging conditions, i.e., acquisition time and scope of the ground meteorological temperatures of the two Landsat images of Shenzhen acquired under similar conditions.

It is assumed that the LST products generated from Landsat-7 and Landsat-8 images exhibit similar spatial patterns and statistical UHI results. Note that the same procedure, which is elaborated in Section 3, was employed to generate the LST products and UHI results for both Landsat images. The obtained UHI maps are shown in Fig. 1, and the corresponding statistical results are presented in Table 2.

A similar spatial pattern can be observed between the two images in Fig. 1; however, according to the statistical results in Table 2, there are significant differences, particularly for the weak UHI type, which had a difference of 6.15 %. It is clear that the LST products from different Landsat images cannot be directly combined for long-term analysis. Therefore, it is necessary to study the consistency of heterogeneous Landsat LST products and build relationships between LST products from different Landsat images for long-term UHI applications.

2.2. Study area

This study was conducted in Shenzhen, China, which is located in the Guangdong province, between 113°46′E–114°37′E, and 22°24′N–22°52′N (Fig. 2). The city has a subtropical climate with generally high summer temperatures, frequent rains from April to September, and relatively dry conditions in other seasons. The city has an average annual temperature of 22.4 °C and there are ten districts in Shenzhen that cover 1997.47 km^2, of which 927.96 km^2 are built-up areas.

In this study, a long-term analysis of the UHI effect in Shenzhen during autumn was conducted from 2014 to 2019 using multisource Landsat images. For most years, an appropriate Landsat-8 image was obtained (considering that the cloud cover ratio is <5 % and the acquisition time should be in autumn), except for 2018, in which year there is no image fulfilling these rules. Therefore, a contemporaneous Landsat-7 image was selected as an alternative for long-term analysis, as shown in Table 3.

Table 1
Imaging conditions of the utilized Landsat images.

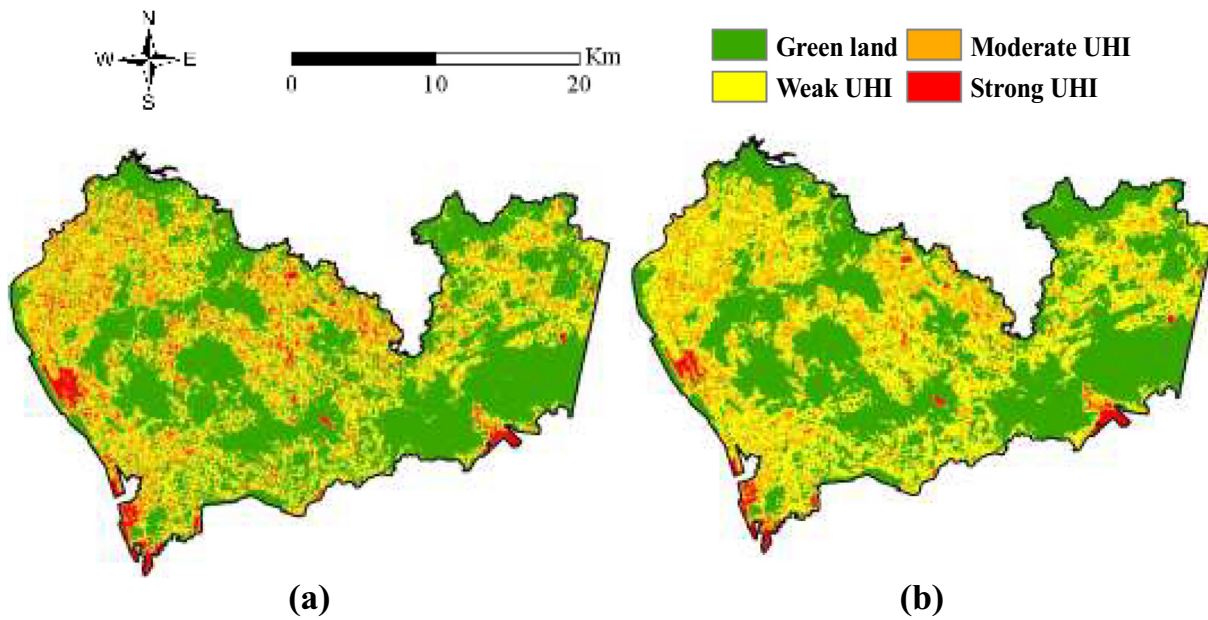| Acquisition time	Satellite	Daily temperature (from meteorological station)	
		Max	Min
2017-10-23 (10:52)	Landsat-8	27 °C	17 °C
2017-10-31 (10:54)	Landsat-7	25 °C	18 °C

Fig. 1. UHI maps generated from (a) Landsat-7 images (October 31, 2017) and (b) Landsat-8 images (October 23, 2017).

Table 2
Statistical results of UHI grade from different Landsat images.

UHI grade	UHI map from Landsat-7 image	UHI map from Landsat-8 image
	Area proportion	Area proportion
Green island	49.86 %	48.92 %
Weak UHI	**28.93 %**	**35.08 %**
Moderate UHI	16.77 %	14.09 %
Strong UHI	4.44 %	1.91 %

Table 3
Characteristics of Landsat images utilized for the UHI effect analysis in Shenzhen.

Date	Satellite	Daily T-max	Daily T-min	Transit time
2014-10-15	Landsat-8	23 ℃	15 ℃	10:54
2015-10-18	Landsat-8	18 ℃	12 ℃	10:51
2016-09-18	Landsat-8	25 ℃	18 ℃	10:54
2017-10-23	Landsat-8	27 ℃	17 ℃	10:52
2018-10-02	**Landsat-7**	**30 ℃**	**24 ℃**	**10:49**
2019-11-14	Landsat-8	25 ℃	19 ℃	10:52

As mentioned in Section 2.1, the consistency of the LST products from different Landsat sensors must be considered. The detailed procedure for establishing the relationship between the LST products from Landsat-7 and Landsat-8 images is detailed as follows.

3. Methodology

The proposed framework for the long-term analysis of the UHI effect using multisource Landsat images is illustrated in Fig. 3.
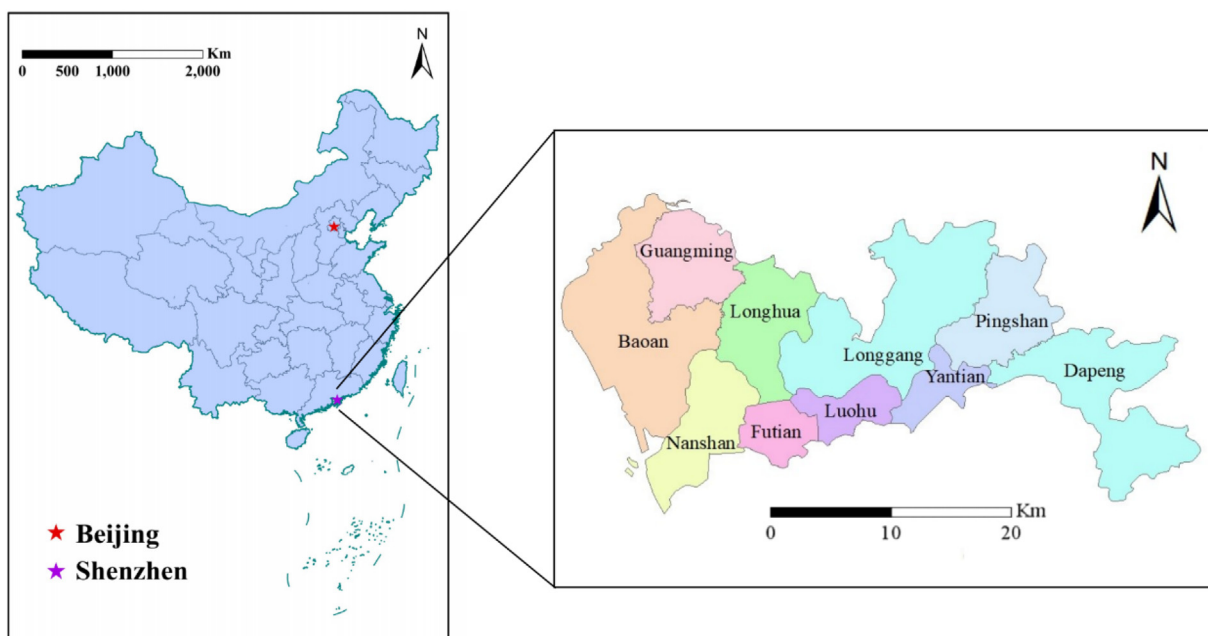

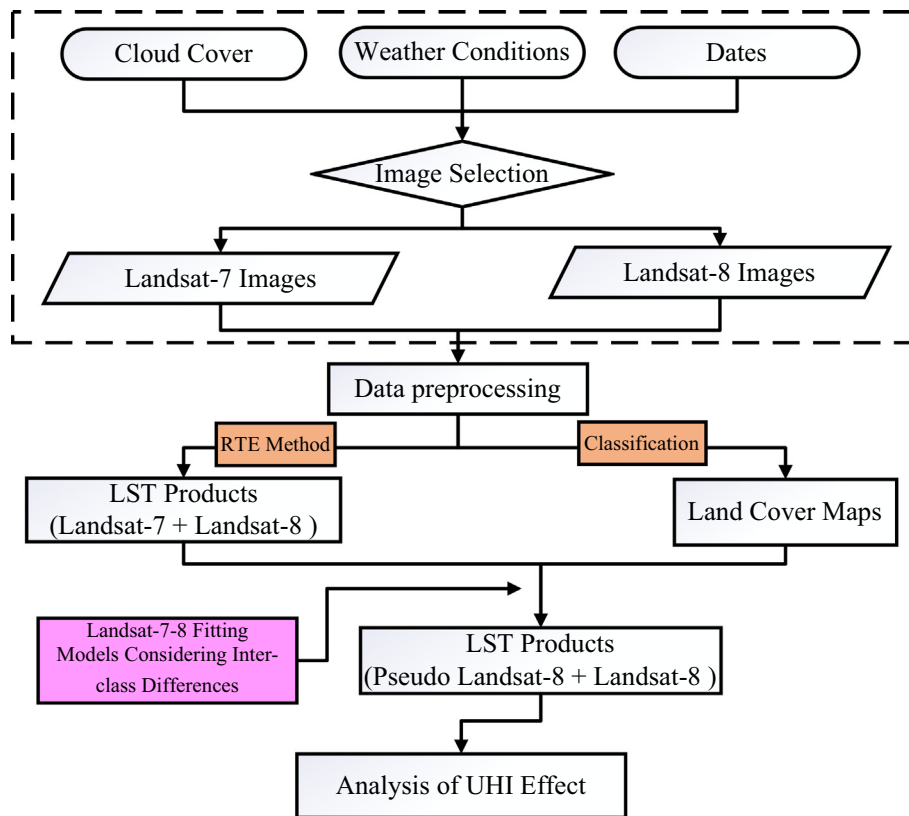**Fig. 2.** Location and administrative regions of the study area (Shenzhen).

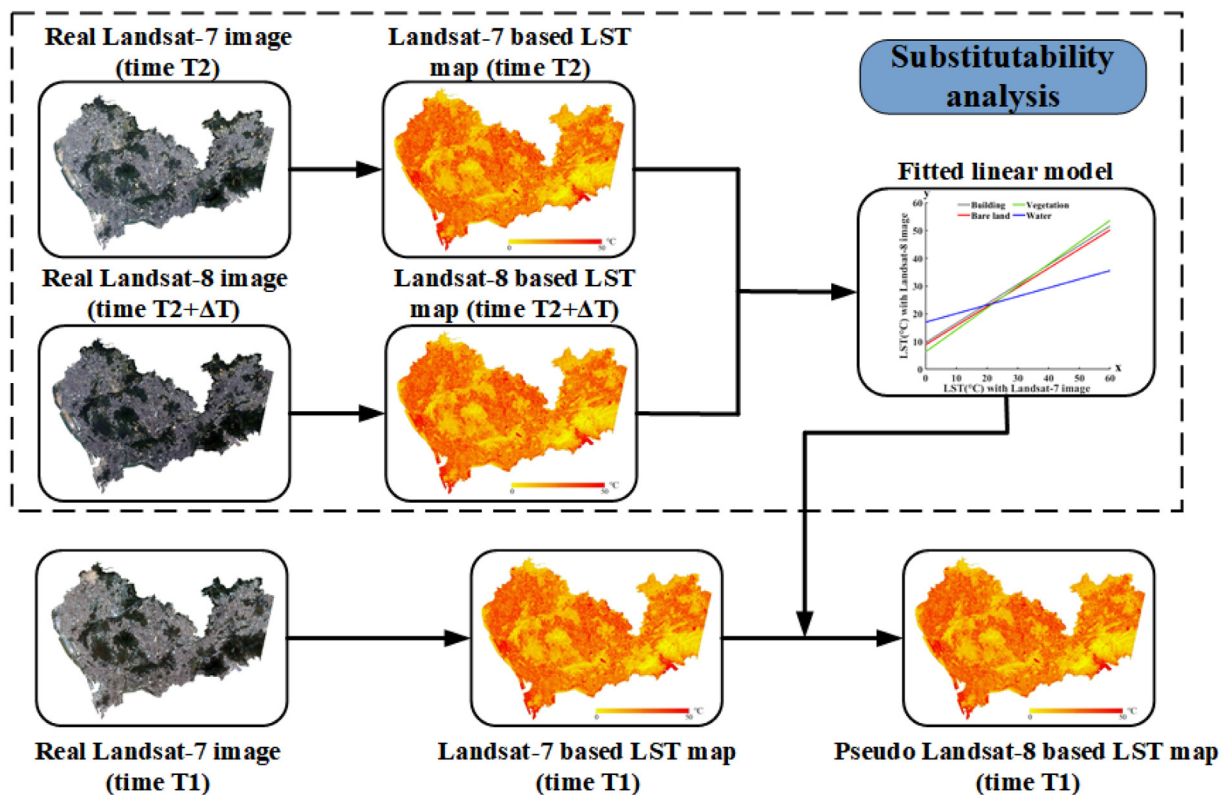**Fig. 3.** Flowchart of the research framework.

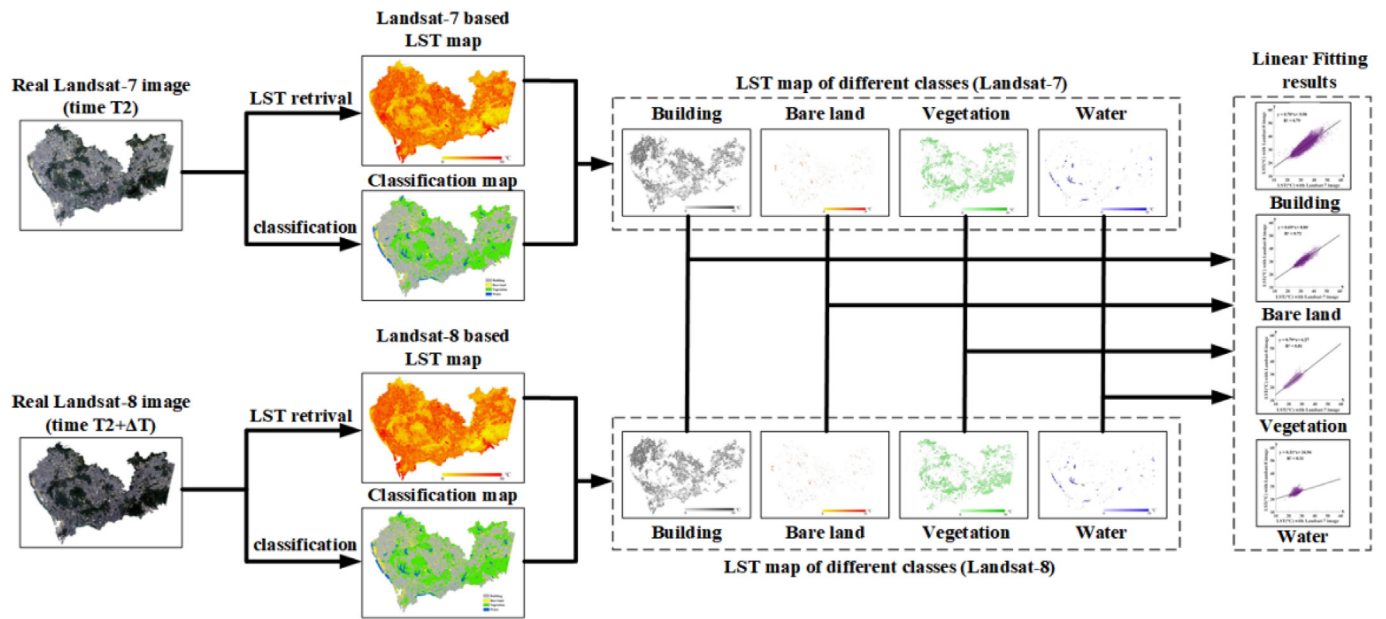**Fig. 4.** Procedure to generate a pseudo Landsat-8-based LST map.

Fig. 5. Relationship (considering the inter-class differences) between the LST products derived from the selected image pair (Landsat-7: 2017-10-31; Landsat-8: 2017-10-23).

3.1. Data preprocessing

Before the LST products were generated, the utilized Landsat images were preprocessed. For the Landsat-7 image, a stripe repair procedure was conducted using ENVI software to refill the dead pixels caused by sensor faults. Radiometric calibration was then implemented for all Landsat images according to the corresponding calibration coefficients.

3.2. LST retrieval

To avoid the impact of different LST retrieval methods on the generated LST products, an identical LST retrieval method was used for both the Landsat-7 and Landsat-8 images. To determine the optimal method for the purpose of this study, four typical LST retrieval methods were compared: the radiative transfer equation (RTE) method (Zhou et al., 2014), image-based method (Zhang et al.,
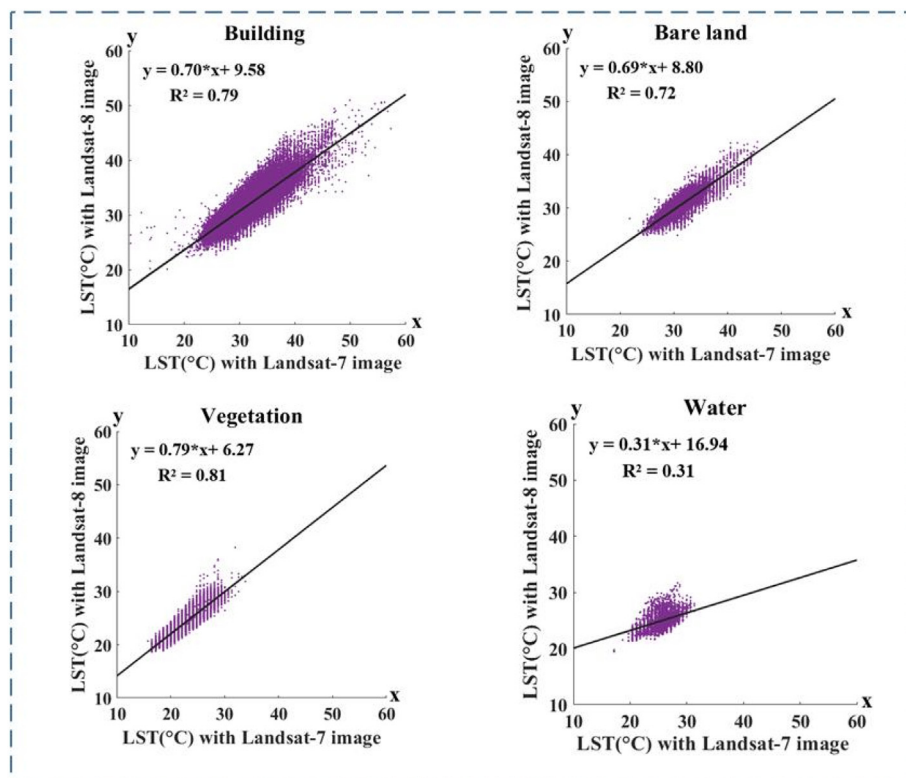

Fig. 6. Fitted linear models of the Landsat image pair.

Table 4
Grading criteria for UHI intensity.

T_R	Grade	UHI intensity
<1.0	1	Green island
1.0–1.1	2	Weak UHI
1.1–1.2	3	Moderate UHI
>1.2	4	Strong UHI

2013), mono-window algorithm (Qin et al., 2001; Wang et al., 2015), and single-channel algorithm (Jiménez-Muñoz & Sobrino, 2003; Jiménez-Muñoz et al., 2014). These methods were reviewed in our

previous research (Xu et al., 2021), which considered the similarities between the generated LST maps from Landsat-7 and Landsat-8 images. It was found that the results from the RTE method exhibited the highest correlation; therefore, this method was chosen to generate the LST products for all Landsat images in this study.

The fundamental principle of the RTE method is that the top-of-atmospheric (TOA) radiance, L_λ, received by the satellite sensors consists of three parts, as shown in Eq. (1) below:

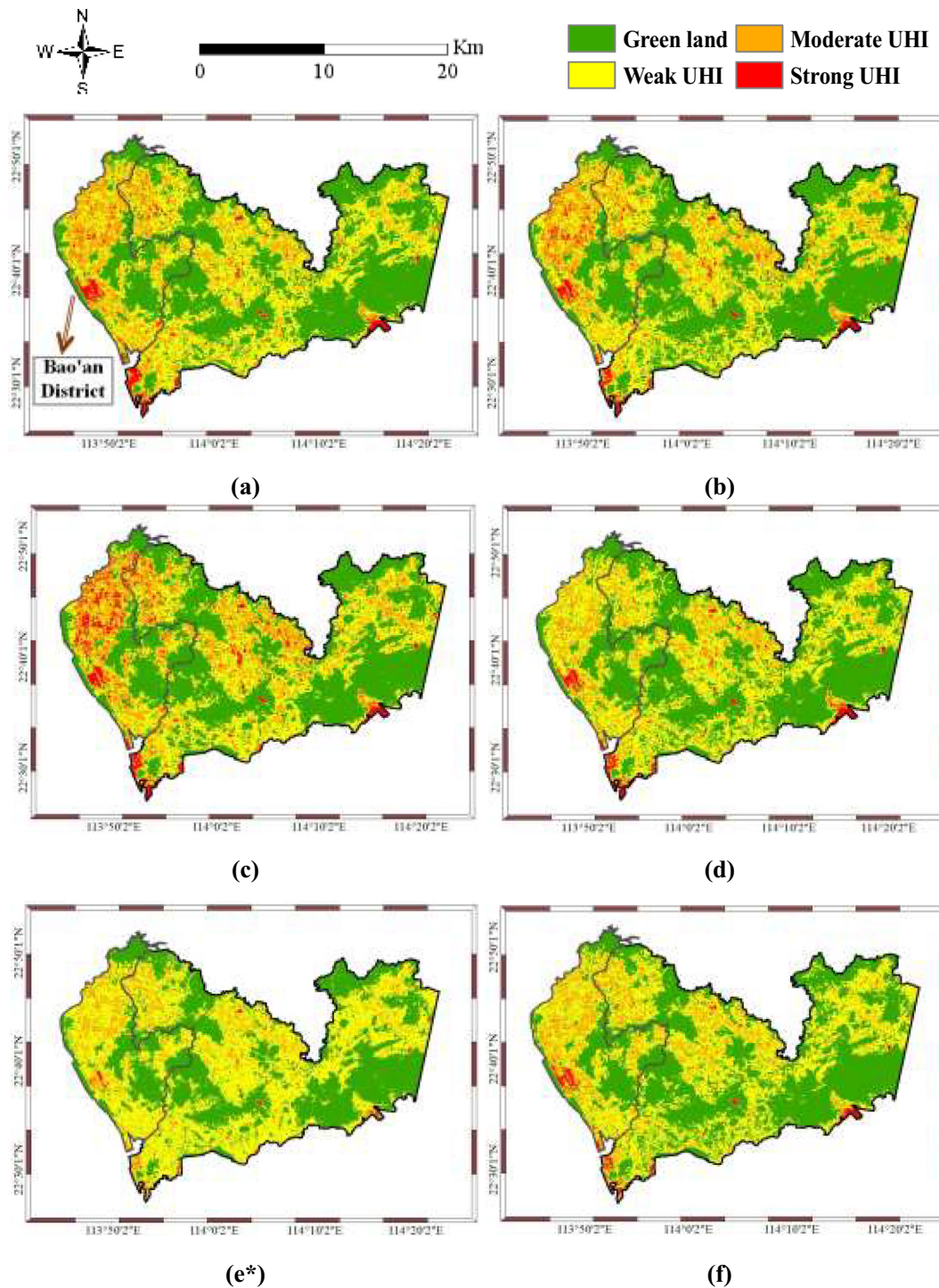$$L_T = \frac{L_\lambda - L_\mu - \tau(1-\varepsilon)L_d}{\tau\varepsilon} \tag{1}$$

Fig. 7. Shenzhen UHI intensity maps for autumn during 2014–2019: (a) 2014-10-15, (b) 2015-10-18, (c) 2016-09-18, (d) 2017-10-23, (e*) 2018-10-02*, and (f) 2019-11-14.

where L_μ is the upwelling (or atmospheric path) radiance; L_T is the surface-leaving radiance of a black body target; and L_d is the downwelling (or sky) radiance. Notably, L_T is the actual radiance emitted from the ground to the satellite sensors after passing through the atmosphere, and it can be used to obtain the LST value using Planck's formula. In this way, the TOA radiance can be converted to surface-leaving radiance by removing the effects of the atmosphere in the thermal region. τ is the atmospheric transmission, which can be obtained in addition to L_u and L_d using the atmospheric correction tool developed by NASA (Barsi et al., 2005); ε is the emissivity of the surface, which is calculated from the normalized difference vegetation index (NDVI) and vegetation coverage ratio.

3.3. Fitting of multisource LST maps

As shown in Table 3, the Landsat-7 image was used to generate the LST map for 2018. Because different sensors were used, a pseudo Landsat-8-based LST product was generated for long-term UHI effect analysis. Thus, a relationship between the LST products from Landsat-7 and Landsat-8 images was built, and the Landsat-7-based LST map was then converted to a pseudo Landsat-8-based LST map, as illustrated in Fig. 4. The key issues in this procedure were 1) how to build a relationship between the LST products from Landsat-7 and Landsat-8 images and 2) to what extent can the fitted model at time T2 be used to replace that at time T1? The selection of the Landsat image pairs at time T2 was important for fitting the model, and its impact is further discussed in Section 5.2.

In this study, for the given Landsat-7 image (2018-10-02), a Landsat image pair (Landsat-7: 2017-10-31; Landsat-8: 2017-10-23) was selected. Then, a linear fitting model was constructed to describe the relationship between these multisource LST products, considering the inter-class differences, as shown in Fig. 5. In this way, the fitted model was used to convert the Landsat-7-based LST product to a pseudo Landsat-8-based LST product for the long-term analysis of the UHI effect.

In addition, support vector machines (SVM) classifier (Hermes et al., 1999) was utilized to generate classification maps for all Landsat images used in this study, which consisted of four typical land cover types (building, bare land, vegetation, and water). To reduce the impact of classification errors on the linear model fitting procedure, only pixels belonging to the same class and corresponding classification probabilities higher than 0.97 in both Landsat-7 and Landsat-8 classification images were selected to fit the linear model. Moreover, pixels located in the striped area of the Landsat-7 image were excluded. The fitted linear models are shown in Fig. 6.

The coefficient of determination, R^2, was selected to evaluate the fit of the linear model; R^2 refers to the degree of fit of the regression line to the set of observed values, as described in Eq. (2) below:

$$R^2 = \frac{\sum_{i=1}^n (\widehat{y}_i - \overline{y})^2}{\sum_{i=1}^n (y_i - \overline{y})^2} \tag{2}$$

where y_i is the observed value; $\overline{y}$ is the mean of all y_i values; and $\widehat{y}_i$ is the fitted value.

3.4. UHI intensity grading

The generated LST products are related to the daily temperature and must be further graded to reduce the impact of temperature fluctuations on long-term analysis. Therefore, a relative temperature metric was introduced, as given in Eq. (3) below (Zhao & Ye, 2009):

$$T_R = T/T_{mean} \tag{3}$$

where T_R is the relative temperature; T is the generated LST value; and T_{mean} is the mean LST map value. Eq. (3) was used to generate a grade map, in which four grades can be distinguished (Table 4).

4. Results and discussion

4.1. Spatiotemporal distribution of the UHI intensity for 2014–2019

With the generated LST map fitting model from the Landsat image pair in 2017, the used Landsat-7-based LST product in 2018 can be converted to a pseudo Landsat-8-based LST product in 2018. Combined with other Landsat-8-based LST products from 2014 to 2019, a long-term analysis of the UHI effect in Shenzhen was conducted. The final UHI products from 2014 to 2019 are shown in Fig. 7, where * indicates that a pseudo Landsat-8-based LST product was used.

By comparing the UHI intensity maps for autumn during the period 2014–2019 (Fig. 7), it was found that the UHI intensity was higher in the western region of Shenzhen than in the eastern region. However, the UHI intensity exhibited an apparent decreasing trend after 2016 in the northwest of Shenzhen, i.e., Bao'an District. According to the statistics, the green area in Bao'an District was stable during the period 2014–2016 but increased by 2882.4918 hm^2 in 2017 (from 35,853.0682 hm^2 to 38,735.5600 hm^2), for which the green coverage ratio (GCR) of the urban area increased correspondingly (http://www.baoan.gov.cn/batjj/gkmlpt/content/9/9501/post_9501086.html#24031).

Consequently, it is assumed that the increase in the green areas in Bao'an District contributed to the decrease in the UHI intensity in Shenzhen in 2017, which subsequently transformed some areas with moderate and strong UHI grades into weak UHI grades.

The change in the proportion of each UHI grade in Shenzhen from 2014 to 2019 is shown in Fig. 8. The proportion of green land was relatively stable, with a slight increase in 2017, which attributed to the lower UHI intensity in that year. The proportion of weak UHI intensity decreased continuously from 2014 to 2016 but increased significantly by 5.84 % in 2017 and then remained stable. In contrast, the proportion of moderate and strong UHI intensity grades both increased at first and then decreased from 2014 to 2019; this may have resulted from policies governing urban greenspace protection, thus increasing the GCR in Shenzhen.

According to the UHI intensity maps between 2014 and 2019, the areas of moderate and strong UHI intensities are mainly located in the central and western regions of Shenzhen, as well as some built-up areas along the coast. For the eastern region, the UHI intensity tended to increase from the coastal areas to inland areas, which may be related to the fact that the focus of economic development has been shifting to inland areas in Shenzhen. After 2017, the UHI intensity maintained the distribution pattern of "strong-
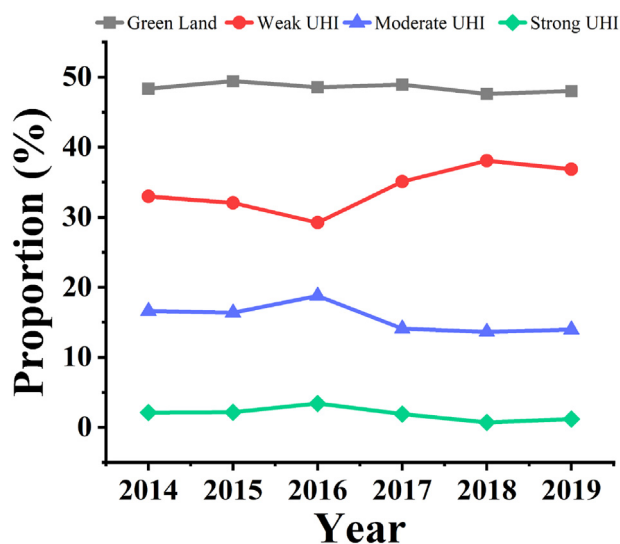

Fig. 8. Proportion of each UHI intensity grade in Shenzhen from 2014 to 2019.
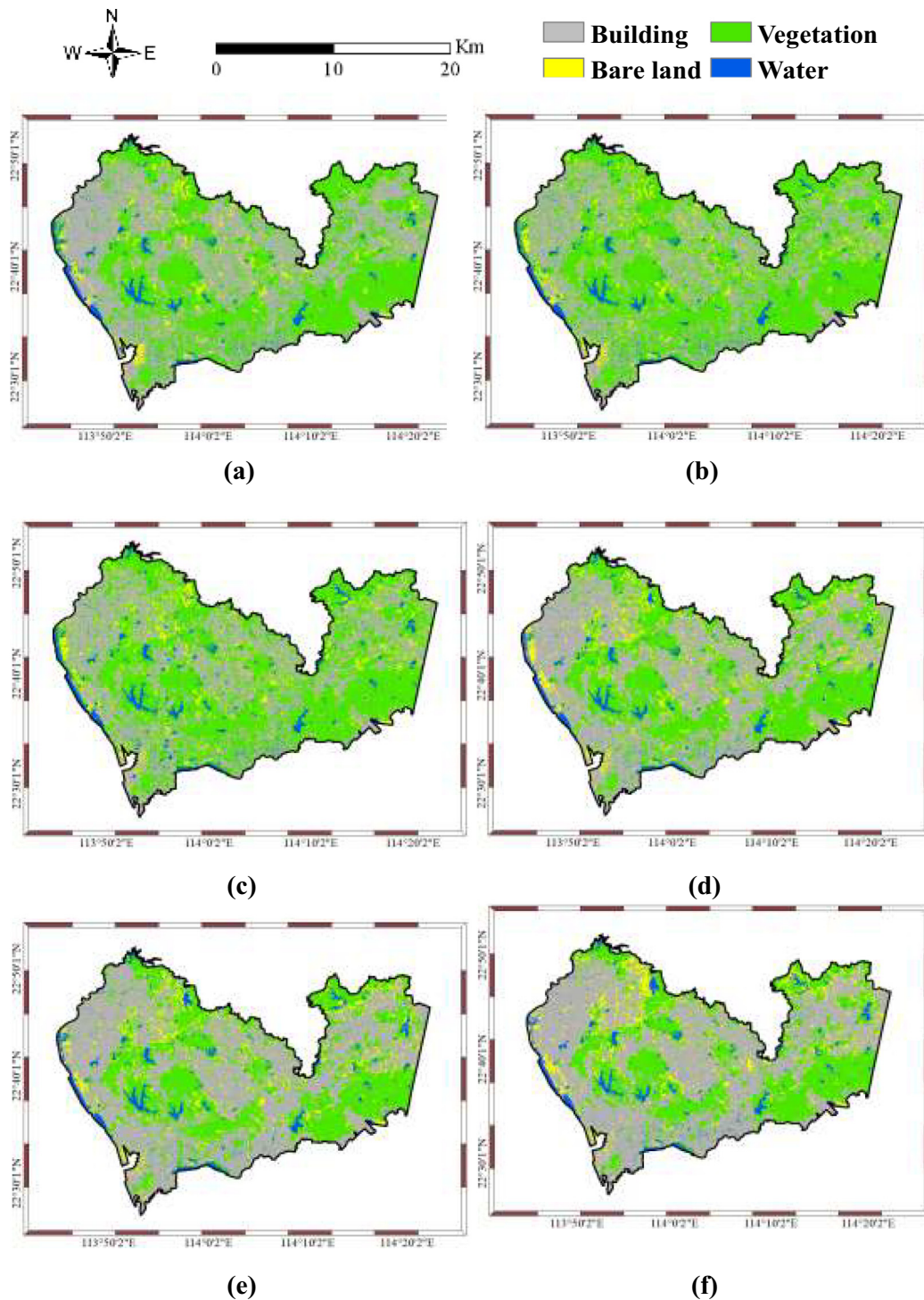
Fig. 9. Land cover maps of Shenzhen during the period 2014–2019: (a) 2014-10-15, (b) 2015-10-18, (c) 2016-09-18, (d) 2017-10-23, (e) 2018-10-02 (Landsat-7), and (f) 2019-11-14.

central, weak-east, and moderate-west," with a significant decrease in UHI intensity in the western area.

4.2. Relationship between UHI intensity and land cover types

To study the relationship between UHI intensity and land cover types, the SVM classification method was used to classify all Landsat images used in this study. The land cover maps generated for Shenzhen during the period 2014–2019 are shown in Fig. 9, in which a Landat-7 based classification map was used for year 2018 owing to that there is no appropriate Landsat-8 image as mentioned before.

The analysis of the UHI intensity and land cover maps shows that most of the green land areas are mountains, forests, and reservoirs, such as Tanglang Mountain, Yangtaishan Forest Park, and Tiegang Reservoir. Strong UHI intensities were mostly located in built-up areas, including ports or transportation hubs along the coast, such as Bao'an International Airport, DaChan Bay Terminals, and Longhua Industrial Zone (Fig. 10).
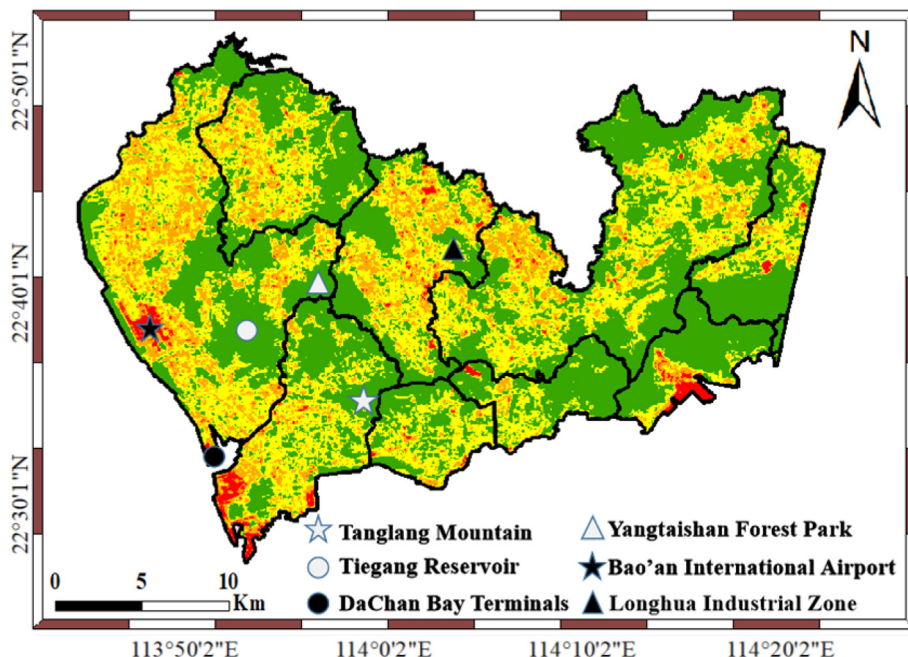
Fig. 10. Typical regions of green land and strong UHI intensities.

Since it was found that the spatial distribution of the UHI intensity in Shenzhen was highly consistent with that of the built-up areas, a statistical correlation analysis was conducted between the LST products and land cover maps. Similar conclusions can be drawn from Fig. 11: the average temperature was highest in built-up areas, followed by bare land, and lowest for water and vegetation types. Moreover, similar average temperatures were noted for water and vegetation land cover types.

The proportions of different land cover types in all the UHI intensity grades between 2014 and 2019 are given in Fig. 12; this further highlights the relationship between the UHI intensity and typical land cover types as follows: Building is the dominant land cover type in all strong and moderate UHI intensity areas, which indicates that building is a major factor to consider when attempting to mitigate the UHI effect in Shenzhen.
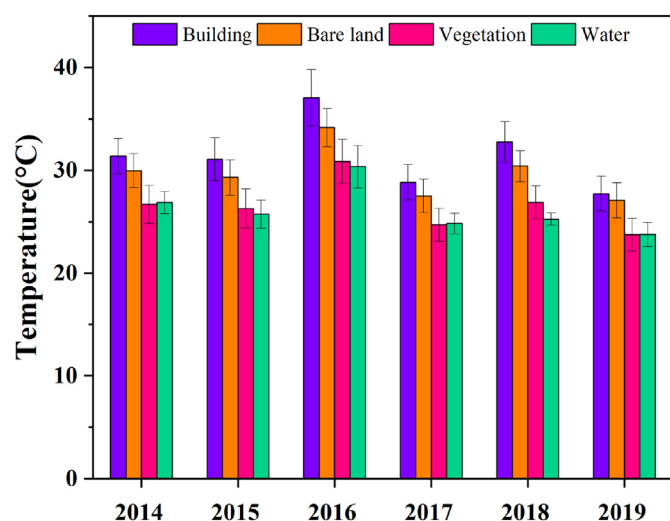
In addition to the impact of rapid urbanization, the introduction of new types of construction materials will benefit the urban thermal environment. Moreover, a large gap of proportion was observed between vegetation and other land cover types in the green land type. A similar tendency was observed for water, which showed a relatively high percentage in green land than in the other three UHI grades. It is therefore believed that both vegetation and water can help mitigate the UHI intensity; hence, there is a need to improve the proportions of vegetation and water in urban areas.

4.3. Relationship between UHI intensity and road networks

In addition to the traditional land cover types, the road network, which is commonly identified as an impervious surface (building and bare land), was considered to qualitatively and quantitatively discuss its relationship with the UHI intensity (as discussed in other studies; Kwak et al. (Kwak et al., 2020)). For convenience, transportation networks of different types, such as railways and highways (Fig. 13 (a)), were rescaled to generate a density map with a spatial resolution of 30 m (Fig. 13(b)), which is the same resolution as the UHI intensity map (Fig. 13(c)).

As shown in Fig. 13(b), areas with a high density of road networks were mainly located in a few districts, such as Bao'an and Nanshan. It can be observed that there was a high consistency between the spatial distribution of road network and the UHI intensity, where areas with a high density of road networks generally exhibited a stronger UHI intensity.

To analyze this relationship quantitatively, 100 discrete points were randomly and evenly selected from the study area. The UHI intensity (T_R) and road network density of these points from the period 2014–2019 were fitted with a linear model, as illustrated in Fig. 14. It can be seen that there was a significantly positive correlation between the density of the road networks and UHI intensity.

4.4. Necessity of using a pseudo Landsat-8-based LST product

To confirm the rationality of replacing the original Landsat-7-based LST product with the pseudo Landsat-8-based LST product for 2018, a

Fig. 11. Statistical analysis of LST for different land cover types during 2014–2019.
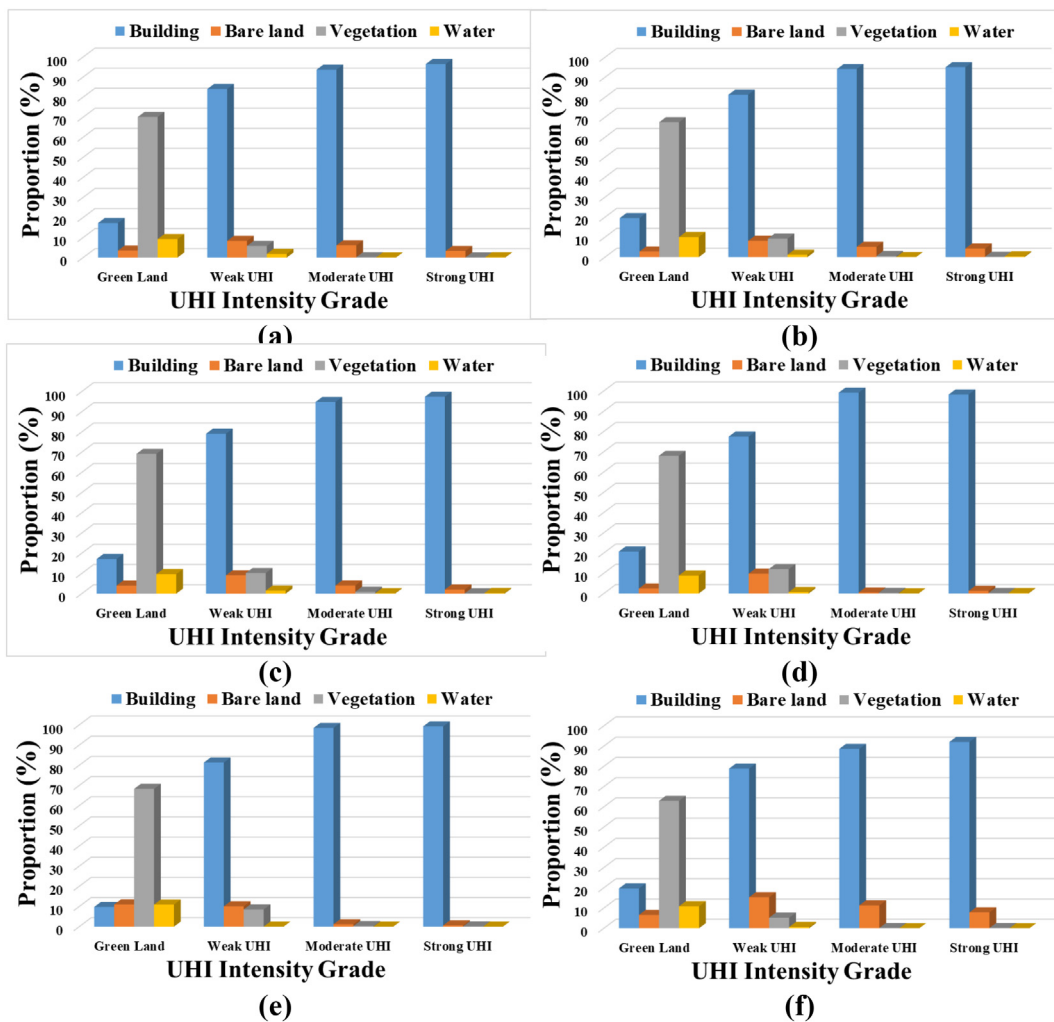
Fig. 12. Relationship between UHI intensity grades and land cover types in (a) 2014, (b) 2015, (c) 2016, (d) 2017, (e) 2018, and (f) 2019.

comparative experiment was conducted, and the results are shown in Fig. 15. It can be observed that when the Landsat-7-based LST product for 2018 was used for analysis, the proportion of the moderate UHI intensity increased accompanied by a decrease in the weak UHI intensity, indicating an exacerbation of the UHI effect. However, when the pseudo Landsat-8-based LST product was used, as in this study, an opposite conclusion can be drawn: the UHI intensity was mitigated in 2018.

Therefore, a MODIS-based LST product (date: 2018-10-02) was utilized to verify the proposed strategy of this study. The Landsat-7-based and pseudo Landsat-8-based LST products were firstly resampled to the same spatial resolution as the MODIS-based LST product. After that, the correlation coefficient index was calculated between the Landsat-based LST products and the MODIS-based LST product. It is shown that the correlation coefficient with the pseudo Landsat-8-based LST product is a little higher than that of Landsat-7-based LST product (0.682 and
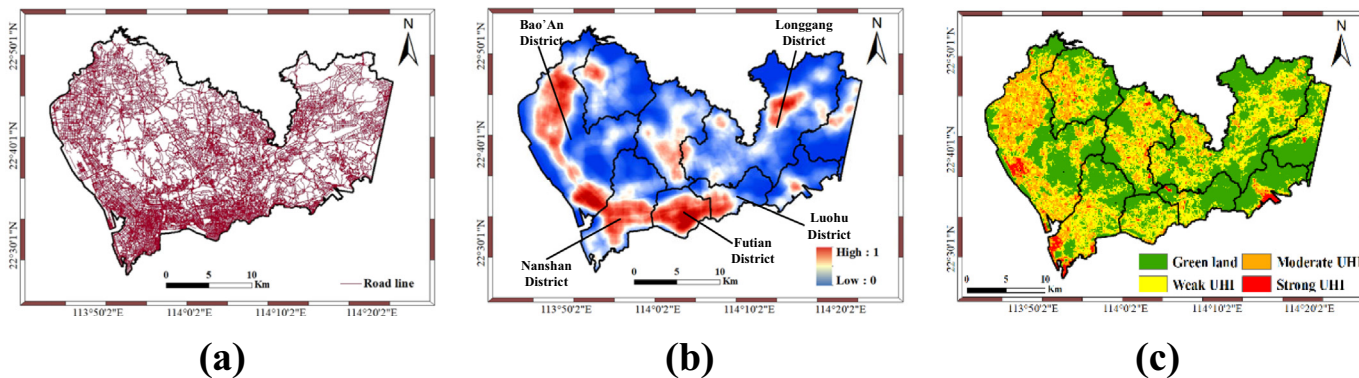

Fig. 13. Road maps of Shenzhen: (a) road networks and (b) density map and (c) the UHI intensity map for 2014 (2014-10-15).
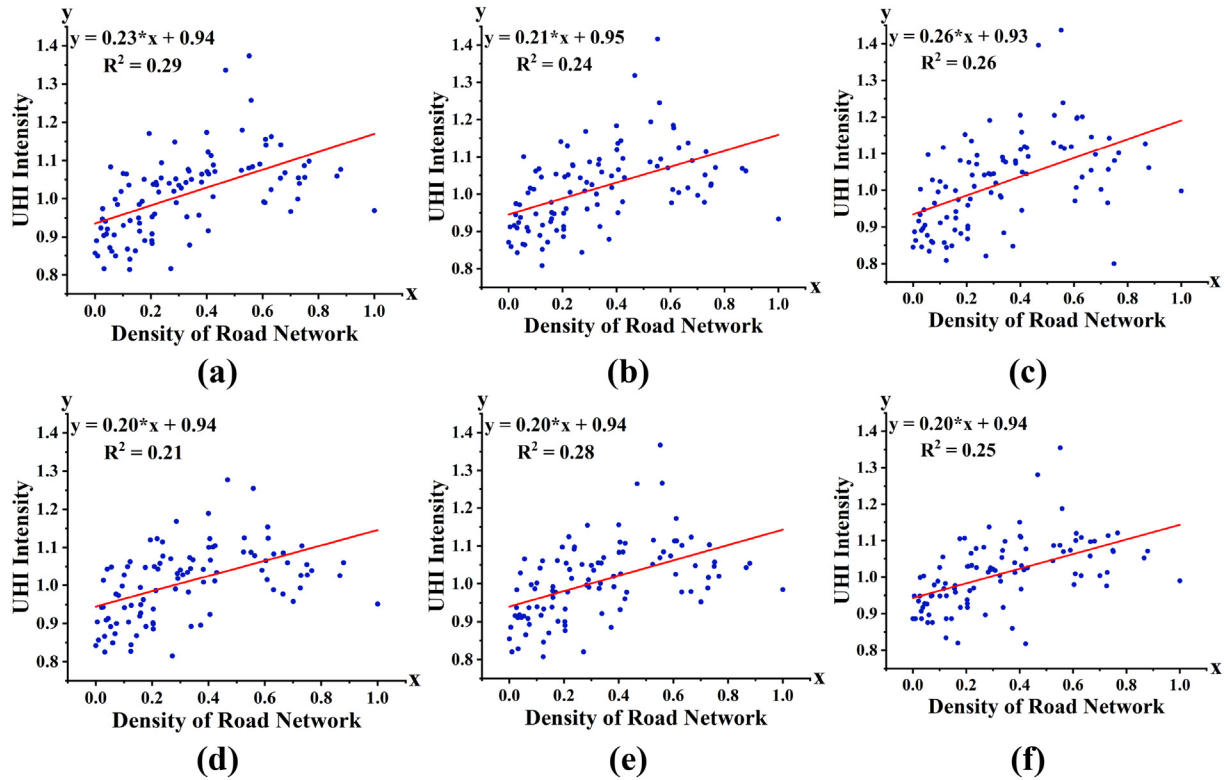
Fig. 14. Relationship between UHI intensity and road network density in (a) 2014, (b) 2015, (c) 2016, (d) 2017, (e) 2018, and (f) 2019.

0.678 respectively), which means that it is reasonable to consider the differences in multisource LST products for long-term analysis of the UHI effect.

4.5. Suggestions on mitigating the UHI effect

Given the above qualitative and quantitative analyses, some suggestions can be made to mitigate the UHI intensity in Shenzhen. As urban construction planning, building, and other impervious surfaces are the main contributors to the UHI effect, the proportion of urban buildings should be reasonably restricted according to environmental conditions. For example, the direction of main roads could be consistent with the dominant wind direction of the city. The expansion of construction land in central urban areas should also be controlled to effectively prevent the concentration of excessive population in urban areas. Moreover, greening utilities, such as

the new 3-D green volume (Zheng et al., 2021), could be further increased to counter the negative impacts of impervious surfaces on the UHI effect.

5. Sensitivity analysis

As illustrated in Fig. 4, a fitting model at time T2 was employed to generate a pseudo Landsat-8-based LST product for time T1, where the actual Landsat-8 image was not accessible. It was evident that the selection of Landsat image pairs at time T2 was an important factor in the fitted model; however, a key issue was then identified—to what extent can the fitted model at time T2 be used to replace that at time T1? In this section, different factors, including land cover and seasonal and inter-annual differences, which may influence the fitted model, were considered. In addition, a similarity index was designed to measure the similarity between the different fitting models.
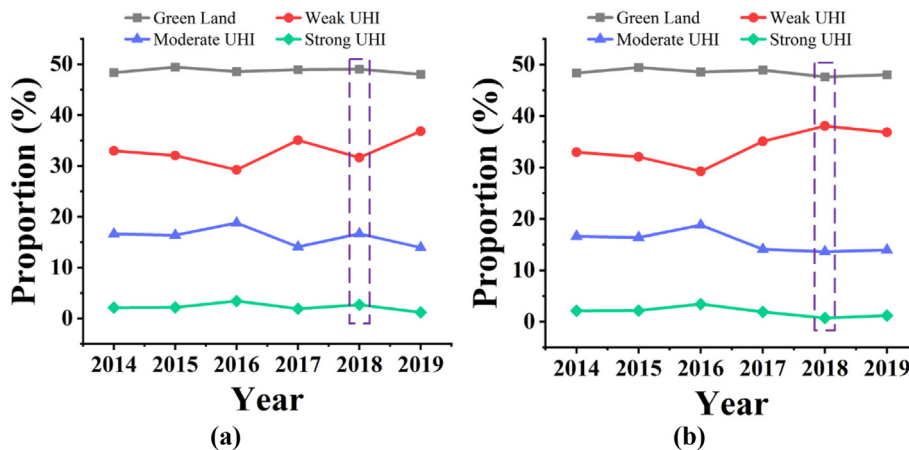

Fig. 15. Proportion of each UHI intensity grade in Shenzhen for the period 2014–2019 using (a) the Landsat-7-based and (b) pseudo Landsat-8-based LST product in 2018 for analysis.
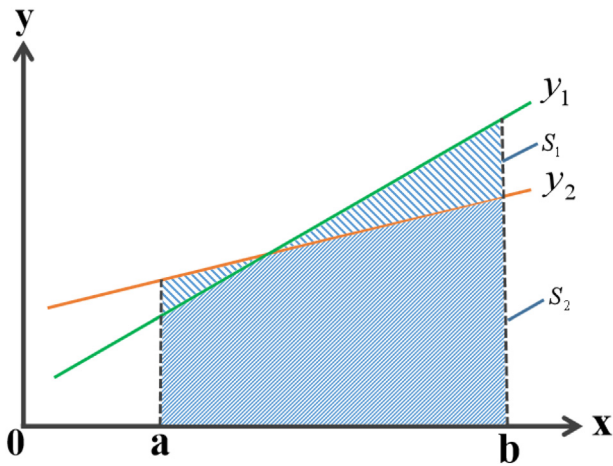
Fig. 16. An illustration of the similarity index *S*.

Table 5
Landsat image pairs selected for substitutability analysis of fitted models.

Image pair	Date	Satellite	Daily T-max	Daily T-min	Transit time
1	2016-03-02	Landsat 7	23 °C	15 °C	10:54
	2016-03-26	Landsat 8	18 °C	12 °C	10:51
2	2017-10-31	Landsat 7	25 °C	18 °C	10:54
	2017-10-23	Landsat 8	27 °C	17 °C	10:52
3	2019-11-22	Landsat 7	27 °C	19 °C	10:35
	2019-11-14	Landsat 8	25 °C	19 °C	10:52

5.1. Similarity index between fitted models

As the linear model was employed to depict the relationship between two LST products from the Landsat-7/8 pair, the similarity index, *S*, is given by Eq. (4) to measure the similarity between two fitted models:

$$S = \int_a^b \frac{|y_2 - y_1|}{\min(y_1, y_2)} dx \tag{4}$$

where y_1 and y_2 are the two fitted models, and *a* and *b* are the lower and upper limits of the temperature, which were 0 and 60 °C respectively. It is evident that the smaller the *S* value, the higher the similarity between the fitted linear models, as shown in Fig. 16.

Table 6
Similarity metrics between different land cover types (symmetric matrix).

Landsat-7 (2017-10-31) and Landsat-8 (2017-10-23)

	Building	Bare land	Vegetation	Water
Building	0	0.0343	0.0475	**0.3088**
Bare land	–	0	0.0580	**0.2882**
Vegetation	–	–	0	**0.3647**
Water	–	–	–	0

Landsat-7 (2016-03-02) and Landsat-8 (2016-03-26)

	Building	Bare land	Vegetation	Water
Buildings	0	0.0440	0.0475	**0.2623**
Bare land	–	0	0.0178	**0.2342**
Vegetation	–	–	0	**0.2495**
Water	–	–	–	0

Landsat-7 (2019-11-22) and Landsat-8 (2019-11-14)

	Building	Bare land	Vegetation	Water
Building	0	0.0274	0.1083	**0.1611**
Bare land	–	0	0.1018	**0.1478**
Vegetation	–	–	0	**0.2550**
Water	–	–	–	0

5.2. Data preparation and model generation

To conduct the substitutability analysis of the fitted models, three Landsat image pairs were selected while considering the acquisition time and weather conditions, as shown in Table 5. A fitting model was generated for each image pair. The results showed that there were inter-annual differences between image pairs 2 and 3, while both seasonal and inter-annual differences existed for image pairs 1 and 2 (and image pairs 1 and 3). Based on these collected Landsat image pairs and the designed similarity index, a similarity analysis was performed to determine whether the fitted model generated at time T1 can be replaced with another fitted model generated at time T2.

The LST and classification maps of all Landsat images were generated using the same processing procedure described in Section 3. Furthermore, the fitted linear models for different land cover types for each image pair were obtained, as shown in Fig. 17.

5.3. Substitutability analysis between fitted models

5.3.1. Impact of land cover type

To study the impact of land cover types on fitted models, the designed similarity index in Eq. (4) was used to evaluate the similarity between the fitted models of different land cover types (Table 6).
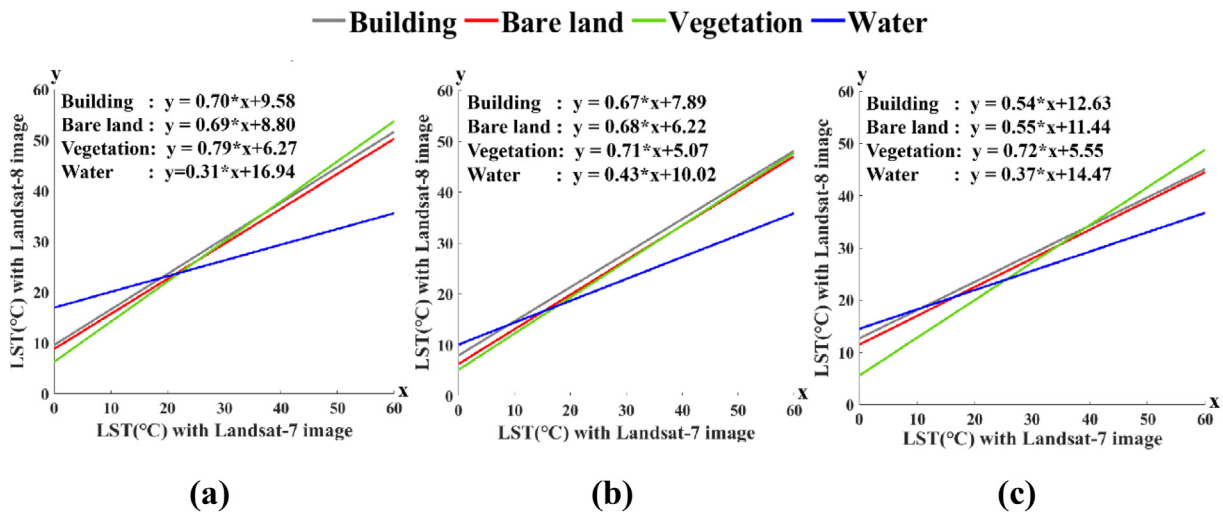

Fig. 17. Linear fitted models for different land cover types for each Landsat image pair: (a) pair 1; (b) pair 2; and (c) pair 3.
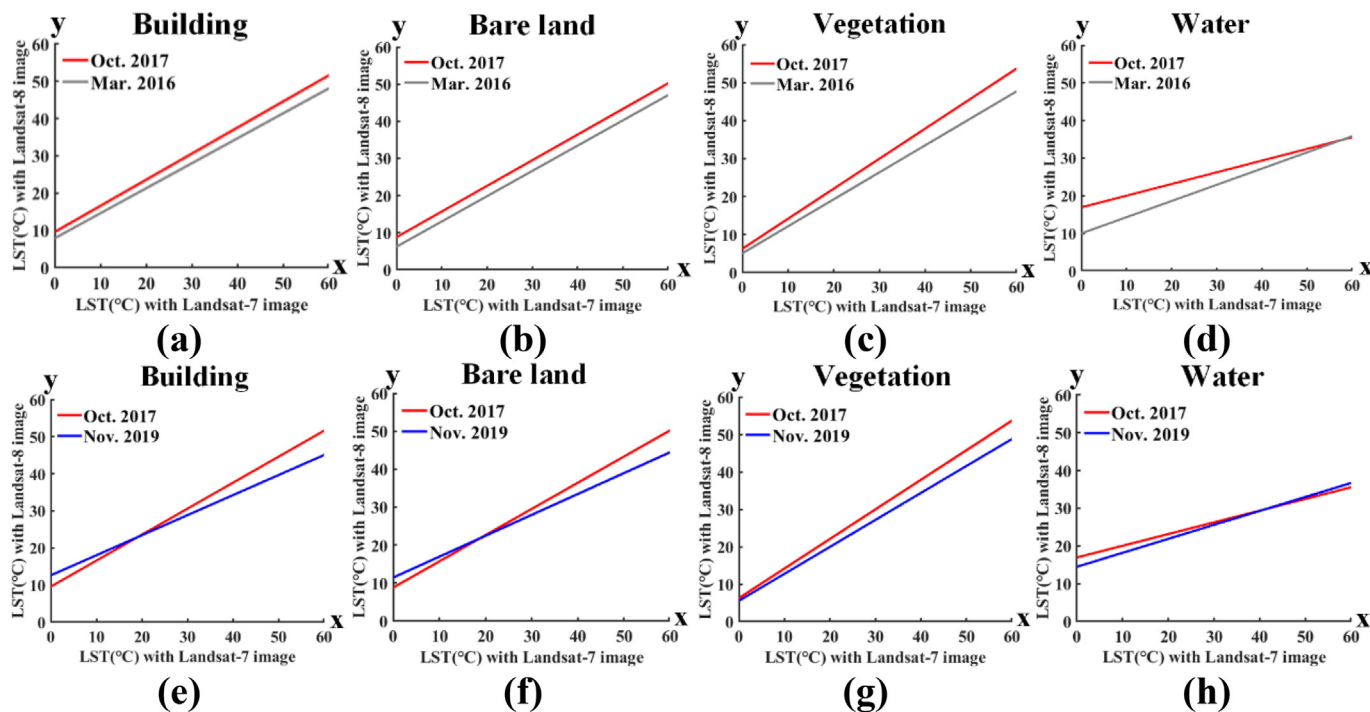
Fig. 18. Fitted models for each land cover type in different seasons and years: (a)–(d) October 2017–March 2016 and (e)–(h) October 2017–November 2019.

Essentially, the S values derived from all combinations of buildings, bare land, and vegetation types were relatively low, which indicates a high degree of similarity between the corresponding fitted models. In contrast, the S values derived from water and the other three land cover types were much higher, indicating poor similarity. As can be seen from Fig. 17, there were relatively larger differences between the fitted models of water and the other three classes; therefore, the land cover types were simply classified into two categories, i.e., water and non-water, to build the fitting models of Landsat LST product pairs for application.

5.3.2. Impacts of seasonal and inter-annual differences on fitted models
Fig. 18 shows the fitted linear models of each land cover type across different seasons and years; these models were used to study the impacts of seasonal and inter-annual differences on fitted models. The similarity between fitted models of each land cover type, with different seasons and years, is illustrated in Table 7.

By comparing the experimental results between October 2017 and November 2019, it can be observed that the S values exhibited a relatively small change for different land cover types, given the inter-annual difference, which indicates that the fitting models generated for the same season of adjacent years have a high degree of similarity. Therefore, it is believed that the impact of inter-annual differences on fitted models is negligible, and the fitted models for the same season of adjacent years can be replaced to some extent.

Table 7
Similarity of each land cover type in different seasons and years.

October 2017–March 2016					
Land cover type	Building	Bare land	Vegetation	Water	S_{mean}
S	0.0874	0.0976	0.1337	0.1195	**0.1096**
October 2017–November 2019					
Land cover type	Building	Bare land	Vegetation	Water	S_{mean}
S	0.1086	0.0979	0.1031	0.0400	**0.0874**

The S values of the fitted models of each land cover type in different seasons were obtained (Table 7), and the fitted models of image pairs 1 (March 2016) and 2 (October 2017) were utilized, and the differences were also small. Given that the inter-annual difference was determined to not be a key factor affecting the fitted model, a similar conclusion can therefore be obtained: In some cases, a fitted model can also be replaced with that of other seasons.

6. Conclusions

In this study, the deviation among multisource Landsat-based LST products and their corresponding impacts on the long-term analysis of the UHI effect were studied. It was found that there were apparent deviations in the retrieved LST results from different sensor data, i.e., Landsat-7 and Landsat-8 images, which were both acquired under similar circumstances in the same region. These deviations resulted from the inherent differences among multisource sensors. Therefore, a fitting model (that indicates a linear relationship between two variables) was built between the LST results generated from the two multisource Landsat sensors. Shenzhen was selected as the study area, and the corresponding Landsat images from 2014 to 2019 were collected, in which a Landsat-7 image was used in 2017 and subsequently converted to a pseudo Landsat-8-based LST product for the long-term analysis of the UHI effect.

By analyzing the spatiotemporal patterns of the UHI intensity in Shenzhen using long-term generated LST products during the period 2014–2019, the relationship between the UHI intensity and road networks was also analyzed. Finally, based on the above discussions, suggestions were made on how to mitigate the UHI intensity in Shenzhen.

Furthermore, the possible impact factors, such as land cover types and seasonal and inter-annual differences, that may affect the fitting models, were analyzed. The constructed fitting model was found to have a strong relationship with land cover types, but a relatively weak relationship with seasonal and inter-annual differences. This means that a pseudo Landsat-8-based LST product can be generated from a Landsat-7-based LST product using the model fitted by a Landsat-7/8 pair obtained in adjacent years or different seasons. The fitting model between Landsat-7 and Landsat-8 images in this study may also be affected by other factors, such as the location

of the study area and the climate types. Currently, owing to the limitation of data acquisition and other factors, we only discussed the applicability of the model in Shenzhen, during autumn 2014–2019. In the future, the applicability of this model to heterogeneous regions or places with rapidly changing features will be further studied.

CRediT authorship contribution statement

Xiong Xu: Conceptualization, Methodology, Writing-reviewing and editing, Supervision. Haoyang Pei: Methodology, Validation, Writing-original draft. Chao Wang: Writing-reviewing and editing, Validation. Qingyu Xu: Formal analysis, Writing-reviewing and editing. Huan Xie: Supervision. Yanmin Jin: Visualization. Yongjiu Feng: Supervision. Xiaohua Tong: Funding acquisition, Project administration. Changjiang Xiao: Data curation.

Data availability

Data will be made available on request.

Declaration of competing interest

The authors declare that they have no known competing financial interests or personal relationships that could have appeared to influence the work reported in this paper.

Acknowledgements

References

Barsi, J.A., Schott, J.R., Palluconi, F.D., Hook, S.J., 2005. Validation of a web-based atmospheric correction tool for single thermal band instruments[C]//Earth observing systems X. SPIE 5882, 136–142.

Cheng, C., Cai, Z., Yan, W., Li, H.Y., Meng, W.Q., Hao, C., Mo, X.Q., 2010. Study of temporal and spatial variation of urban heat island based on landsat TM in central city and binhai new area of Tianjin. Journal of Natural Resources. 25 (10), 1727–1737.

Clinton, N., Gong, P., 2013. MODIS detected surface urban heat islands and sinks, global locations and controls. Remote Sens. Environ. 134, 294–304.

Cui, H.S., Qian, L.X., 2010. A study of the relation between the land use types and urban heat island effect in Guangzhou city based on remote sensing. IEEE Int. Conf. Image Anal. Sign. Process. 460–465.

Ding, H., Shi, W., 2013. Land-use/land-cover change and its influence on surface temperature, a case study in Beijing City. Int. J. Remote Sens. 34 (15), 5503–5517.

Estoque, R.C., Murayama, Y., 2017. Monitoring surface urban heat island formation in a tropical mountain city using landsat data (1987–2015) [J]. ISPRS J. Photogramm. Remote Sens. 133, 18–29.

Hermes, L., Frieauff, D., Puzicha, J., Buhmann, J.M., 1999. Support vector machines for land usage classification in landsat TM imagery. IEEE Int. Geosci. Rem. Sens. Symp. 348–350.

Howard, L., 1833. The climate of London: deduced from meteorological observations made in the metropolis and at various places around it[M]. Harvey and Darton, J. and A. Arch, Longman, Hatchard, S. Highley [and] R. Hunter.

http://www.baoan.gov.cn/batjj/gkmlpt/content/9/9501/post_9501086.html#24031, n.d.

Hu, H.L., Chen, Y.H., Gong, A.D., 2005. Advance in the application of remotely sensed data to the study of urban heat island[J]. Rem. Sens. Land Resour. 17 (3), 5–9.

Jiménez-Muñoz, J.C., Sobrino, J.A., 2003. A generalized single-channel method for retrieving land surface temperature from remote sensing data[J]. Journal of Geophysical Research: Atmospheres. 108 (D22).

Jiménez-Muñoz, J.C., Sobrino, J.A., Skoković, D., Mattar, C., Cristobal, J., 2014. Land surface temperature retrieval methods from Landsat-8 thermal infrared sensor data[J]. IEEE Geosci. Remote Sens. Lett. 11 (10), 1840–1843.

Kaplan, G., Avdan, U., Avdan, Z.Y., 2018. Urban heat island analysis using the landsat 8 satellite data, a case study in Skopje, Macedonia. Multidiscip. Dig. Publ. Inst. Proc. 2 (7), 358.

Kumar, K.S., Bhaskar, P.U., Padmakumari, K., 2012. Estimation of land surface temperature to study urban heat island effect using LANDSAT ETM+ image[J]. International Journal of Engineering Science and Technology. 4 (2), 771–778.

Kwak, Y., Park, C., Deal, B., 2020. Discerning the success of sustainable planning: a comparative analysis of urban heat island dynamics in korean new towns[J]. Sustain. Cities Soc. 61, 102341.

Li, X., Ding, J.L., Wang, G., Zhang, Y.J., Zhang, Z., Yan, X.Y., 2014. Change of LUCC and characteristic of landscape pattern in a typical oasis in Turkmenistan[J]. J. Dess. Res. 34 (1), 260–267.

Liu, C.C., Cao, G.Z., Zhang, M.W., Niu, X.Z., Xu, W.B., Fan, J.L., 2013. Influence of temporal and spatial variability on estimation of air temperatures from MODIS land surface Temperatures[J]. Rem. Sens. Technol. Appl. 28 (3), 463–482.

Liu, Z.H., 2017. Spatio-temporal variation characteristics of urban heat islands in Hefei City, Anhui Province of China based on spatio-temporal fusion[D]. Anhui University.

Mohajerani, A., Bakaric, J., Jeffrey-Bailey, T., 2017. The urban heat island effect, its causes, and mitigation, with reference to the thermal properties of asphalt concrete. J. Environ. Manag. 197, 522–538.

Mohan, M., Kikegawa, Y., Gurjar, B.R., Bhati, S., Kolli, N.R., 2013. Assessment of urban heat island effect for different land use-land cover from micrometeorological measurements and remote sensing data for megacity Delhi. Theor. Appl. Climatol. 112 (3), 647–658.

Mostovoy, G.V., King, R.L., Reddy, K.R., Kakani, V.G., Filippova, M.G., 2006. Statistical estimation of daily maximum and minimum air temperatures from MODIS LST data over the state of Mississippi[J]. GI Sci. Rem. Sens. 43 (1), 78–110.

Nichol, J., 2005. Remote sensing of urban heat islands by day and night. Photogramm. Eng. Remote Sens. 71 (5), 613–621.

Owen, T.W., Carlson, T.N., Gillies, R.R., 1998. An assessment of satellite remotely-sensed land cover parameters in quantitatively describing the climatic effect of urbanization. Int. J. Remote Sens. 19 (9), 1663–1681.

Qin, Z., Karnieli, A., Berliner, P., 2001. A mono-window algorithm for retrieving land surface temperature from landsat TM data and its application to the Israel-Egypt border region [J]. Int. J. Remote Sens. 22 (18), 3719–3746.

Ranagalage, M., Estoque, R.C., Murayama, Y., 2017. An urban heat island study of the Colombo metropolitan area, Sri Lanka, based on landsat data (1997–2017) [J]. ISPRS Int. J. Geo Inf. 6 (7), 189.

Ren, K., Sun, W., Meng, X., Yang, G., Peng, J., Huang, J., 2022. A locally optimized model for hyperspectral and multispectral images fusion. IEEE Trans. Geosci. Remote Sens.

Sultana, S., Satyanarayana, A.N.V., 2020. Assessment of urbanisation and urban heat island intensities using landsat imageries during 2000–2018 over a sub-tropical Indian City [J]. Sustain. Cities Soc. 52, 101846.

Sun, W., Liu, K., Ren, G., Liu, W., Yang, G., Meng, X., Peng, J., 2021. A simple and effective spectral-spatial method for mapping large-scale coastal wetlands using China ZY1-02D satellite hyperspectral images. Int. J. Appl. Earth Obs. Geoinf.

Tan, M., Li, X., 2013. Integrated assessment of the cool island intensity of green spaces in the mega city of Beijing. Int. J. Remote Sens. 34 (8), 3028–3043.

Vancutsem, C., Ceccato, P., Dinku, T., Connor, S.J., 2010. Evaluation of MODIS land surface temperature data to estimate air temperature in different ecosystems over Africa[J]. Remote Sens. Environ. 114 (2), 449–465.

Wang, F., Qin, Z., Song, C., Tu, L., Karnieli, A., Zhao, S., 2015. An improved mono-window algorithm for land surface temperature retrieval from landsat 8 thermal infrared sensor data[J]. Remote Sens. 7 (4), 4268–4289.

Xu, H.Q., Chen, B.Q., 2004. A study on urban heat island and its spacial relationship with urban expansion: Xiamen, SE China[J]. Urban Stud. 2, 65–70.

Xu, Q.Y., Xu, X., Xie, H., Zhang, X.C., Huang, Y.T., 2021. A new strategy for comparison of land surface temperature retrieval methods with landsat remote sensing images considering regional Consistency[C]. IOP Conf. Ser. Earth Environ. Sci. IOP Publ. 687 (1), 012166.

Yang, P., Chen, J., Hou, X.W., Gao, Q., Zhao, Q., 2013. Study of urban heat island based on multi-source data-by the example of the Shijiazhuang area[J]. Meteorol. Month. 39 (10), 1304–1313.

Yusuf, Y.A., Pradhan, B., Idrees, M.O., 2014. Spatio-temporal assessment of urban heat island effects in Kuala Lumpur metropolitan city using landsat images. Journal of the Indian Society of Remote Sensing. 42 (4), 829–837.

Zhang, H., Qi, Z.F., Ye, X.Y., Cai, Y.B., Ma, W.C., Chen, M.N., 2013. Analysis of land use/land cover change, population shift, and their effects on spatiotemporal patterns of urban heat islands in metropolitan Shanghai, China[J]. Appl. Geogr. 44, 121–133.

Zhao, X.F., Ye, H., 2009. Monitoring the changes of urban heat island seasonal dynamics in the process of urbanization by remote sensing. Ecol. Environ. Sci. 18 (5), 1817–1821.

Zheng, S., Meng, C., Xue, J., Wu, Y., Liang, J., Xin, L., Zhang, L., 2021. UAV-based spatial pattern of three-dimensional green volume and its influencing factors in lingang New City in Shanghai, China[J]. Front. Earth Sci. 15 (3), 543–552.

Zhou, W.Q., Qian, Y.G., Li, X.M., Li, W.F., Han, L.J., 2014. Relationships between land cover and the surface urban heat island, seasonal variability and effects of spatial and thematic resolution of land cover data on predicting land surface temperatures[J]. Landsc. Ecol. 29 (1), 153–167.

Zoran, M., 2012. MODIS and NOAA-AVHRR l and surface temperature data detect a thermal anomaly preceding the 11 march 2011 Tohoku earthquake. Int. J. Remote Sens. 33 (21), 6805–6817.